Cold vacuum chamber for diagnostics: Analysis of the measurements at the Diamond Light Source and impedance bench measurements

R. Voutta,[*] S. Gerstl,[†] S. Casalbuoni,[‡] A. W. Grau, T. Holubek, and D. Saez de Jauregui

IBPT, Karlsruhe Institute of Technology, P.O. Box 3640, D-76021 Karlsruhe, Germany

R. Bartolini, M. P. Cox, E. C. Longhi, G. Rehm, J. C. Schouten, and R. P. Walker

Diamond Light Source, Oxfordshire OX11 0DE, England

M. Migliorati

Department Energetica, University "La Sapienza", Via Antonio Scarpa 14, I-00161 Roma, Italy

B. Spataro

INFN-LNF, Via E. Fermi, 40 00044 Frascati, Roma, Italy

The beam heat load is an important input parameter needed for the cryogenic design of superconducting insertion devices. Theoretical models taking into account the different heating mechanisms of an electron beam to a cold bore predict smaller values than the ones measured with several superconducting insertion devices installed in different electron storage rings. In order to measure and possibly understand the beam heat load to a cold bore, a cold vacuum chamber for diagnostics (COLDDIAG) has been built. COLDDIAG is equipped with temperature sensors, pressure gauges, mass spectrometers as well as retarding field analyzers which allow to measure the beam heat load, total pressure, and gas content as well as the flux of particles hitting the chamber walls. COLDDIAG was installed in a straight section of the Diamond Light Source (DLS). In a previous paper the experimental equipment as well as the installation of COLDDIAG in the DLS are described [S. Gerstl *et al.*, Phys. Rev. ST Accel. Beams **17**, 103201 (2014)]. In this paper we present an overview of all the measurements performed with COLDDIAG at the DLS and their detailed analysis, as well as impedance bench measurements of the cold beam vacuum chamber performed at the Karlsruhe Institute of Technology after removal from the DLS. Relevant conclusions for the cryogenic design of superconducting insertion devices are drawn from the obtained results.

I. INTRODUCTION

Superconducting insertion devices (SCIDs) are employed in different synchrotron light sources in order to increase the offered photon flux and brilliance with respect to permanent magnet based insertion devices. The beam heat load is needed for designing the cooling system of SCIDs. All SCIDs installed in different synchrotron light sources show a beam heat load higher than the one expected [1–5]. A cold vacuum chamber equipped with different diagnostics (COLDDIAG) has been developed to measure and possibly understand the beam heat load to a cold bore. COLDDIAG consists of one cold and two warm sections. All three sections are provided with temperature

sensors and heaters to measure the beam heat load, with gauges to measure the pressure, with mass spectrometers to measure the gas content, and with retarding field analyzers (RFAs) to measure the flux and spectrum of low energy particles impinging the wall. The vacuum chamber seen by the electron beam resembles the one of a SCID.

In a previous paper [6] a detailed description of the instrumentation equipment of COLDDIAG is presented together with the first results obtained at the Diamond Light Source (DLS).

This one presents the following. In the first section we report on the main results of the analysis of the measurements performed with COLDDIAG during one year of operation from September 2012 to August 2013 in the DLS storage ring. The second section focuses on the description of the method and the results of impedance bench measurements, performed at the Karlsruhe Institute of Technology (KIT) after the removal of COLDDIAG from the DLS. The results described in the first two sections are then summarized and discussed. At the end conclusions are presented, including the implications on the cryogenic design of SCIDs.

[*]robert.voutta@kit.edu
[†]stefan.gerstl@kit.edu
[‡]sara.casalbuoni@kit.edu

II. ANALYSIS OF THE MEASUREMENTS PERFORMED AT THE DLS

COLDDIAG was installed in the DLS storage ring from September 2012 to August 2013. During this period measurements were performed for a wide range of machine conditions, employing the various measuring capabilities of the device. In the following, the analysis of the measured beam heat load, pressure and gas content, as well as the low energy charged particle flux and spectrum, as a function of the electron beam parameters (i.e. bunch charge, number of bunches, bunch length and bunch spacing) and COLDDIAG parameters (i.e. liner temperature) is presented, preceded by a summary of the beam parameters and operation modes utilized in the DLS storage ring. A description of the experimental setup is omitted here, since it is extensively described in Ref. [6].

A. The DLS beam parameters and operation modes

The main machine parameters of the DLS are listed in Table I. During the time COLDDIAG was installed in the DLS storage ring two main operation modes were run for user operation: (i) standard mode: average beam current $I = 300$ mA in 900 consecutive bunches with a bunch length of 15.8 ps; (ii) hybrid mode: average beam current $I = 300$ mA in 685 consecutive bunches with a bunch length of 16.6 ps and one higher charge bunch.

In the machine physics sessions special operation modes could be used.

Beam current ramps.—Instead of injecting directly to the maximum beam current for a specific filling pattern, the injection can be paused at intermediate values of the beam current. A waiting time of 15 up to 30 minutes before continuing the injection allows one to measure the beam heat load at the respective beam current.

Equally spaced bunches.—The following filling patterns have been used with different bunch spacings: $I = 60$ mA and 36 bunches with 52 ns separating time, $I = 72$ mA and 52 bunches with 36 ns separating time, $I = 88.3$ mA and 78 bunches with 24 ns separating time, $I = 108$ mA and 117 bunches with 16 ns separating time, and $I = 153$ mA and 234 bunches with 8 ns separating time.

Variable bunch length.—The bunch length was changed by setting a different rf voltage in the accelerating cavities of the storage ring while keeping the bunch charge constant. The bunch length corresponding to each different

TABLE I. Machine parameters of the Diamond Light Source [7].

Electron beam energy	3 GeV
Nominal beam current	300 mA
Circumference	561.6 m
Revolution frequency	533.818 kHz
rf frequency	499.654 MHz
Maximum number of bunches	936

rf voltage has been measured in a separate run with a streak camera [8].

B. Beam heat load

Possible beam heat load sources are synchrotron radiation, heating caused by the resistive wall and geometric impedances, and electron or ion bombardment. Since the beam heat load due to the different mechanisms mentioned above is characterized by specific dependencies on the different beam parameters, specific experiments to study its dependence on the bunch length, the number of bunches, bunch spacing and bunch charge have been conducted during dedicated machine physics special operation modes. However, synchrotron radiation should be negligible since a collimator shields the walls of the liner from direct photon flux produced in the upstream bending magnet.

The beam heat load discussed in the following refers to the heat load that was measured with the cold liner at a fixed temperature of 20 K. The second approach to measure the beam heat load, i.e. letting the liner warm up by the beam current, gives comparable results, but has the intrinsic disadvantage of an uncontrolled liner temperature and a longer measuring time.

As an overview, in Fig. 1 the beam heat load P_{beam} is shown as a function of the average electron beam current I. The different colors refer to individual measurements, each
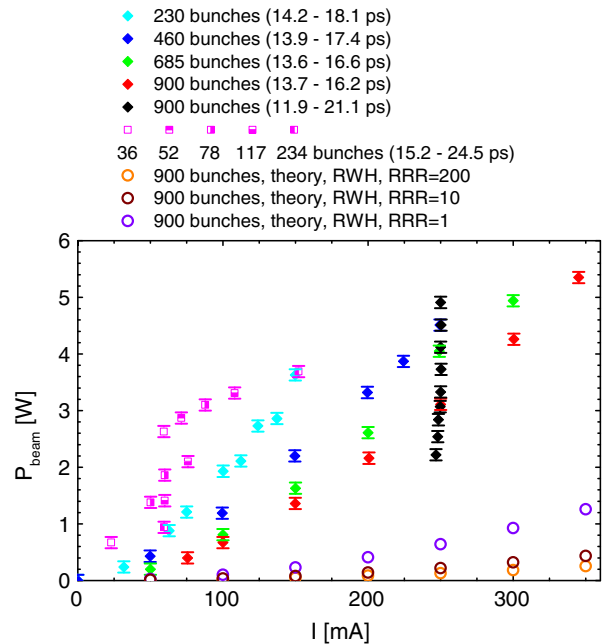

FIG. 1. Beam heat load as a function of the average beam current for a wide range of beam parameters. Included are measurements for four beam current ramps with a certain number of bunches in one train (cyan, blue, green, red), beam current steps for filling patterns with equally distributed bunches (magenta) and a measurement with everything fixed except the bunch length (black). The circles show the expected beam heat load from resistive wall heating for three different purities of copper.

with its respective beam parameter ranges as indicated in the legend. As anticipated in Ref. [6], the measured values are about 1 order of magnitude higher than the ones simulated considering the resistive wall effect in the anomalous skin effect regime of the cold elliptical vacuum chamber for two different purities of copper (orange and dark red open circles). In case of extremely low copper purity, the predicted beam heat load (violet open circles) is about 5 times smaller than the measured one. It can be readily seen that the bunch length has a great impact on the beam heat load (see black diamonds in Fig. 1) and that for the same beam current the beam heat load increases with a higher bunch charge (decreasing number of bunches), as for example at $I = 150$ mA the beam heat load for 230 bunches is about 3 times higher than the heat load for 900 bunches.

Beam heating P_{beam} has different dependencies on the bunch length σ for different radio frequency (rf) effects (geometric and resistive wall impedance). Depending on the particular effect, assuming a longitudinal Gaussian bunch:

$$P_{\text{beam}} \propto \sigma^{-1} \tag{1}$$

for step transitions [9],

$$P_{\text{beam}} \propto \sigma^{-3/2} \tag{2}$$

for resistive wall heating [10],

$$P_{\text{beam}} \propto \sigma^{-5/3} \tag{3}$$

for resistive wall heating in the anomalous regime [11].

In order to distinguish between these different beam heating mechanisms a dedicated measurement has been done, in which the filling pattern was kept the same (250 mA beam current, 900 bunches) and the bunch length was changed by varying the accelerating voltage in the rf cavities of the storage ring. Figure 2 shows the beam heat load measured as a function of the bunch length as well as the fits to the data corresponding to the best fit using a power law and the different rf effects described above. The best fit for the measured data is given by a bunch length dependence of approximately $P_{\text{beam}} \propto \sigma^{-1.4}$ (black line), and by a mixture of heating due to the resistive wall heating in the anomalous skin effect regime and a step (cyan line). For beam heating due to synchrotron radiation one expects no dependence on the bunch length, which is clearly not the case. Beam heating from electron bombardment fits to the general trend of higher beam heat load with shorter bunch length, however the exact dependence is not defined since the underlying beam dynamics is unknown. Thus, beam heating due to electron bombardment cannot be confirmed nor excluded by these observations.

The dependence of the beam heat load on the number of bunches is shown in Fig. 3. Each color stands for a fixed
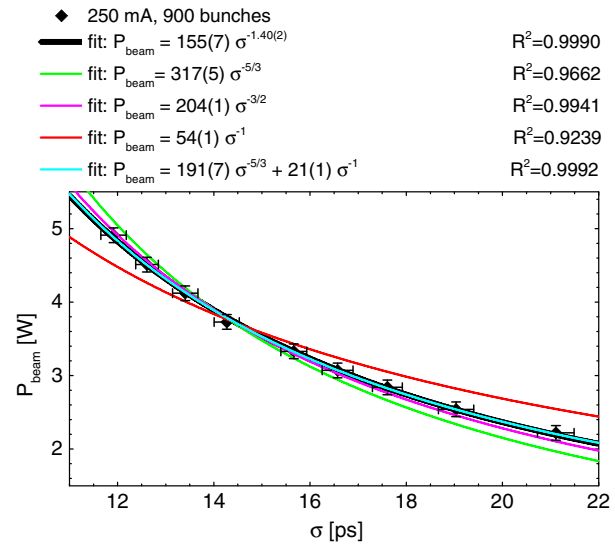

FIG. 2. The measured beam heat load as a function of bunch length for a filling pattern of 250 mA beam current in 900 consecutive bunches is shown together with the fits to the data corresponding to the best fit using a power law and five different rf effects. The adjusted coefficient of determination R^2 is also reported for each fit.

bunch charge and a fixed bunch length. Additionally the bunch spacing has been varied; the red, green and blue points are taken from four different beam current ramps, where the bunches are consecutive in one train with a bunch spacing of 2 ns and a gap of 72, 502, 952, and 1412 ns at the end of the train for the filling pattern with 900, 685, 460 and 230 bunches, respectively. The cyan points are taken from a measurement where the bunch spacing was varied from 8 to 52 ns by distributing the bunches equally along the storage ring.
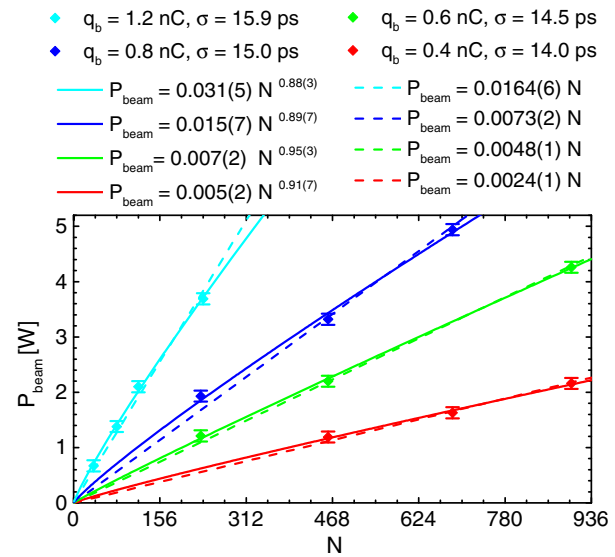

FIG. 3. Beam heat load as a function of the number of bunches for four different bunch charges. For each set a linear fit (dashed line) and a power law (solid line) through the origin is shown.

The best fit to the data using a power law gives an exponent varying between 0.88 and 0.95 (solid line). A linear dependence, which is expected for broadband impedance and synchrotron radiation, is shown as dashed lines. An exponent smaller than one is not consistent with any known theory. Heating from sharp resonances would show a quadratic dependence on the number of bunches and can be excluded.

Models for which the dependence on bunch charge q_b, the number of bunches N and the bunch length σ is known can be fit to the measured data. The best fit is obtained by an empirical model with a dependence on the number of bunches, the bunch length and the bunch charge of $P_{\text{beam}} \propto N^{0.9}\sigma^{-1.4}q_b^{1.82}$ [see Fig. 4(a)]. The other three models in Figs. 4(b) to 4(d) represent heating due to resistive wall heating in the normal and anomalous regime and due to step transitions, respectively. A linear fit is done for each case to test the validity of the model. Comparing the adjusted coefficients of determination R^2, the best fit to the data is given by the empirical model. Both the two resistive wall heating models show less agreement with the data than the empirical one, with the anomalous resistive wall heating model deviating from the data more in the center. The step transition model shows the least agreement, especially for the measurement with different bunch lengths and the same filling pattern [black points in Fig. 4(d)].

With the aim of understanding the role played by the cryosorbed gas layer on the beam heat load mechanisms, the dependence of the beam heating on the liner temperature has been measured. In addition, to compare the beam heat load with and without the cryosorbed gas layer, two warm sections with a shorter liner equipped with the same diagnostics as the cold section have been included.

The beam heat load as a function of the cold liner temperature is reported in Fig. 5 for a fixed filling pattern (900 bunches, 300 mA). The measurement has been performed by using the heaters at the cold stage of the cryocooler to raise the base temperature, and the heaters on the cold liner are used for the temperature control. An overall increase in beam heat load with liner temperature can be observed, which is irregular and shows a local minimum between 28 and 30 K. A pressure change is not visible during the measurement and the gas composition shows only a small change at 30 K, where mainly the partial pressure with mass 28 amu increases by about 50%.

Using the warm sections of COLDDIAG it is also possible to measure the beam heat load at room temperature. Since there is no active cooling in the warm sections the time to reach thermal equilibrium is much longer than in the cold section (1 to 2 days). Therefore it is not possible to measure the beam heat load at a constant temperature. For the same reason, data from dedicated measurement sessions cannot be used. Only the ones recorded during user operation, where the same filling pattern is usually kept for several days can be employed to determine the beam heat load to the warm liner.
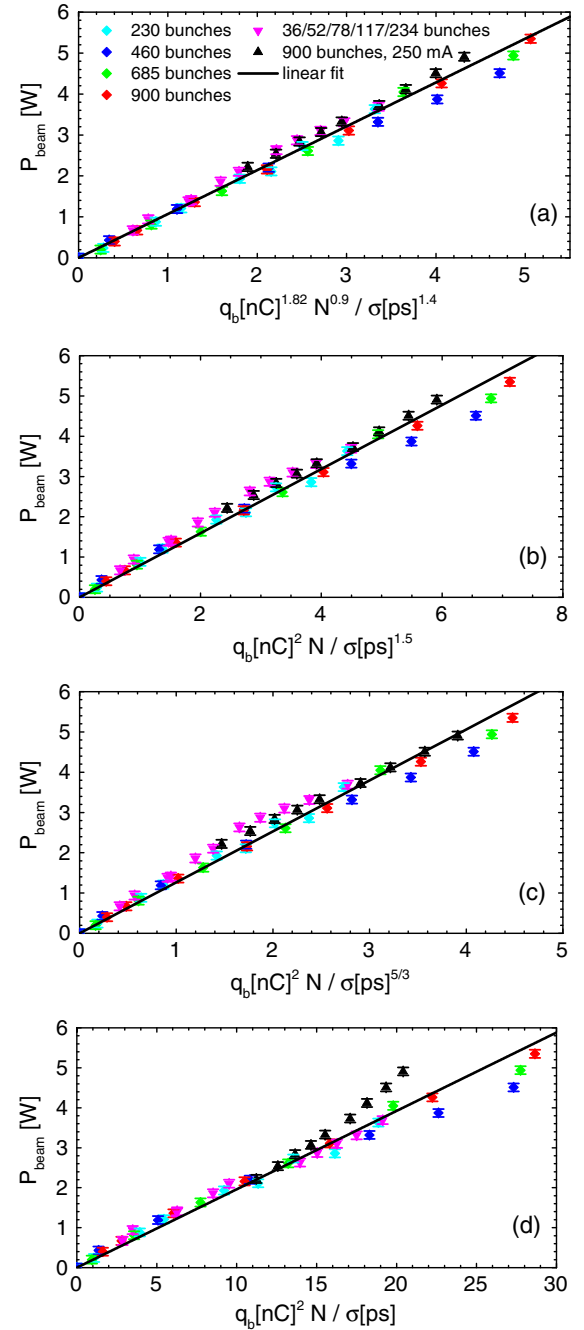

FIG. 4. Comparison of the beam heat load model derived from the measurements and three different rf effect models: (a) empirical with $R^2 = 0.9854$, (b) resistive wall with normal skin effect with $R^2 = 0.9746$, (c) with anomalous skin effect with $R^2 = 0.9712$, (d) step transition with $R^2 = 0.9602$.

The downstream warm section had thermal contact with the cryostat, which lead to a constant temperature in this section (independent of the heat load), preventing the beam heat load determination. The calibration of the upstream warm section is done with the heater on the liner, by heating without beam to the temperature that was measured with beam and reading the power to the heater. In this case the
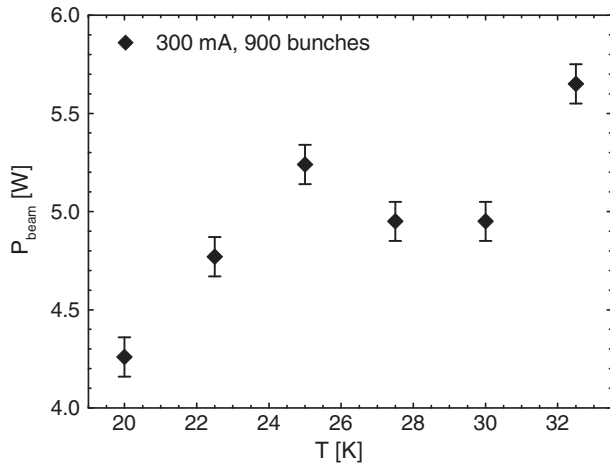
FIG. 5. Beam heat load as a function of the liner temperature at the cooling connection for a fixed filling pattern (300 mA, 900 bunches).

heat coming from the two transitions cannot be removed by a calibration, because there are no temperature sensors at the connecting flanges, and it is therefore included in the measurement.

When comparing the beam heat load in the warm section to the cold section one has to take into account the different lengths of the sections. While the cold section is 0.5 m long, the warm section is only 0.27 m long, and any beam heating effect scaling with length (e.g. resistive wall heating) will scale accordingly. Different heating mechanisms have different dependencies on the length of the heated chamber. For example, resistive wall heating is proportional to the length of the heated liner, while a resonance caused by a specific geometry does not depend on the length of the heated chamber. As a consequence, the comparison between the beam heat load measured in the cold and in the warm section is model dependent. The absolute and scaled beam heat load is shown in Fig. 6 for the upstream warm section and compared to similar measurements in the cold section. The measured beam heat load in the warm section is 30% to 40% lower than in the cold, but when scaled by the length of the section it is 20% to 30% higher. From the two data points for each measured filling pattern it is not possible to identify the specific dependence of the beam heat load measured in the warm sections on the beam current. The measured points can be fit with both a linear dependence $P_{beam} \propto I$ (dashed lines) pointing to synchrotron radiation as heating mechanism, and with a quadratic dependence $P_{beam} \propto I^2$ (solid lines), consistent with a heating mechanism caused by broadband impedance, as in the case of the cold section.

C. Pressure and gas content

The total pressure was measured with the liner temperature in the cold section kept at 20 K. When changing the beam current in the storage ring, the temperatures in the
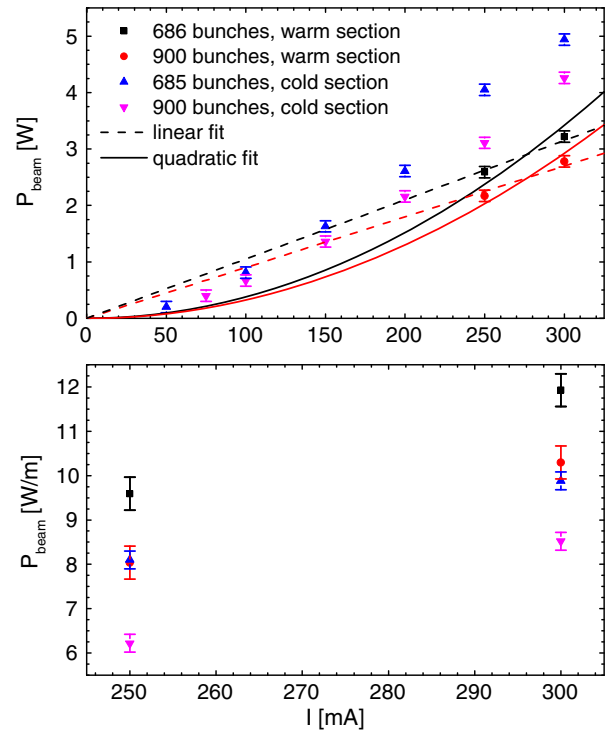

FIG. 6. Comparison between the beam heat load in the warm and in the cold section. Top: measured beam heat load. Bottom: beam heat load scaled by the length of each section. The dashed lines in the upper plot indicate a linear dependence on the beam current $P_{beam} \propto I$, while the solid lines a quadratic one $P_{beam} \propto I^2$.

cryostat as well as the pressures undergo a dynamic change. Therefore the specific pressure values were taken after a waiting time of usually 15 to 30 minutes, which was also needed for the beam heat load measurement, and allows the system to thermally stabilize and yields a value close to the equilibrium pressure.

Figure 7 shows the total pressure as a function of beam current measured for different filling patterns, i.e. beam current ramps with 230, 460, 685 and 900 bunches in one train, several bunch spacings with the bunches distributed equally around the storage ring and different bunch lengths with an otherwise fixed filling pattern (250 mA, 900 bunches), achieved by changing the cavity voltages of the rf system. Unfortunately, the sensitivity of the pressure measurements is limited by outgassing in the diagnostic sections, where the pressure gauges and the RGAs are located. The measured pressure without beam is in the range between 6×10^{-10} and 8×10^{-10} mbar. Within the measured sensitivity, no relevant change in pressure with beam current is observed.

The typical mass spectrum of the residual gas for each of the three sections in COLDDIAG is reported in Fig 8. The spectra were taken with beam (300 mA, 900 bunches), after the pressures and the temperatures have settled from injection, and without beam after the beam dump. The main
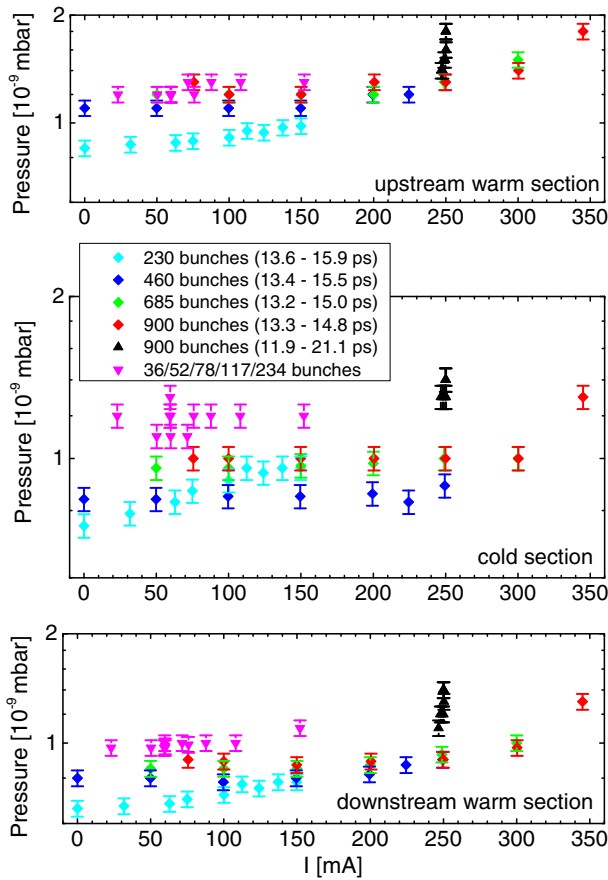
FIG. 7.   Total pressure as a function of beam current in the cold section and the two warm sections of COLDDIAG for several filling patterns. The reproducibility of the pressure reading is 5% [12].
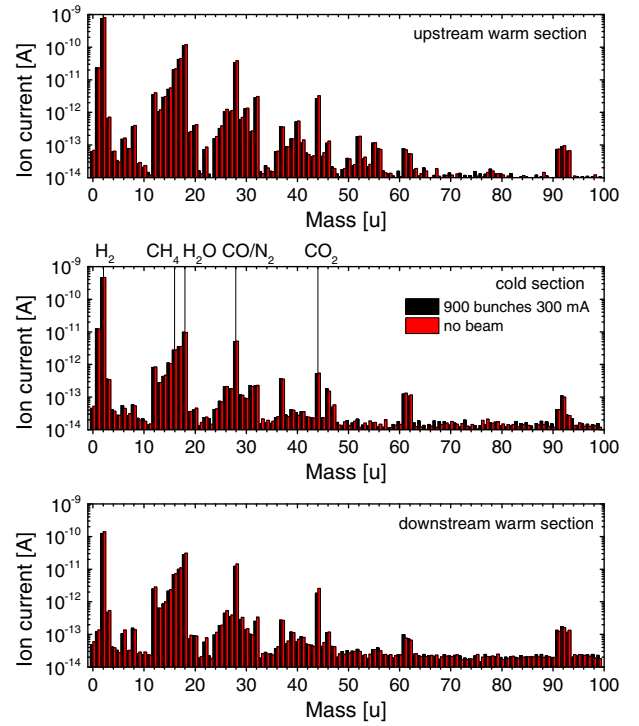

FIG. 8.   Mass spectra of the residual gas in the three sections of COLDDIAG measured with the RGA in each diagnostic port. The measurements with and without beam are 40 minutes apart. Reproducibility of the peak ratio: 0.5%, detection limit: 1×10^{-14} mbar [14].

contributions from hydrogen, water, carbon monoxide/nitrogen, carbon dioxide and methane are indicated. The gas composition looks similar in all three sections and is typical for an unbaked system, dominated by outgassing of the surfaces [13]. In the downstream warm section the background pressure is slightly higher, while in the cold section the contribution from hydrogen relative to water is higher because of the cold surface. In all three sections the presence of the beam has no significant impact on the gas composition.

To answer the question if the pressure has an influence on the beam heat load a test was done, where with beam in the machine, the ion pumps were turned off to generate a pressure increase. The heaters on the liner are set to a power that results in a liner temperature of 20 K. After the pressure has settled from activating the temperature control of the liner, the ion pumps are switched off. This results in a pressure increase in the cold section of roughly 1 order of magnitude from 1×10^{-9} to 1×10^{-8} mbar. Even with 10 times more residual particles in the beam chamber no change in beam heat load can be observed, since the liner temperature as well as the heating power at the liner heaters does not change. This excludes any heating mechanism that

depends on the number of residual gas particles in the beam vacuum, like scattering of bending magnet radiation on the gas particles. It does however not exclude heating originated from the cryosorbed gas layer, because in this case the pressure rise is only a consequence and not the source of the heating.

D. Electron and ion bombardment of the chamber walls

By changing the polarity of the grid voltage and the collector voltage of the RFAs it is possible to differentiate between particles with a positive and a negative charge. With the grid grounded, a negative potential at the collector allows one to collect positively charged ions and a positive potential at the collector is used to collect negatively charged particles. Since the flux of positive ions is an order of magnitude smaller than for electrons [15], we concentrate in the following on measurements of electrons hitting the wall.

Figure 9 shows the measurements for the flux of electrons hitting the chamber walls for three different beam current ramps in the three sections of COLDDIAG. The electron flux is increasing linearly with beam current, but with a different slope in each section. In the upstream warm section the least amount of electrons is detected, whereas in
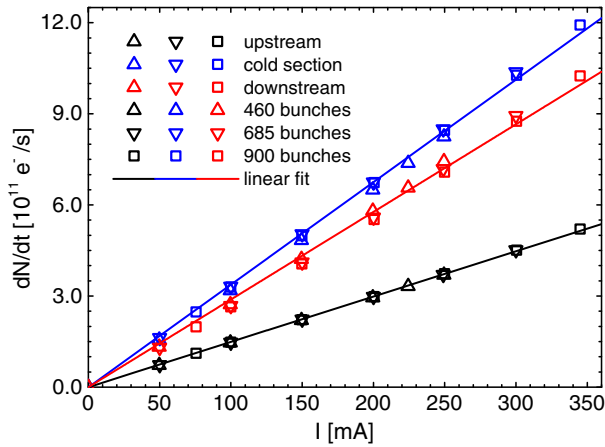
FIG. 9. Flux of negatively charged particles (electrons) as a function of beam current for three different beam current ramps in each of the three sections of COLDDIAG. Accuracy of the current measurement: $\pm0.1\% + 0.1$ nA [16].
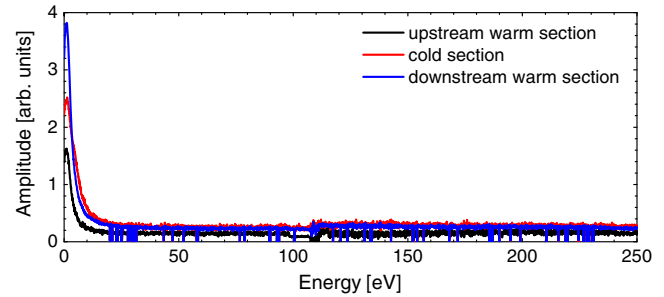

FIG. 10. Energy spectrum of negatively charged particles (electrons) in each section of COLDDIAG for energies up to 250 eV (energy resolution: 0.1 eV). Filling pattern: 250 mA average beam current, 685 bunches, 16 ps bunch length.

the downstream warm section about twice as much is measured, and even more in the cold section.

The linear increase of the collector current with beam current can be explained with photoelectrons, which are produced by synchrotron radiation. Although an upstream absorber should screen all sections of COLDDIAG from synchrotron radiation, it is still possible for reflected synchrotron radiation to reach the liner surface. The measured electron flux is lower in the upstream warm section, because it is closer to the absorber and therefore less illuminated by the reflected synchrotron radiation. From this point of view the electron flux in the downstream warm section would be the highest. It can be higher in the middle cold section because the cryosorbed gas layer can act as an additional source of low energy electrons.

With COLDDIAG it is possible to measure for the first time also the spectrum of low energy electrons impinging the wall in cold conditions [6]. Previous experiments with a dedicated cold vacuum chamber to measure the beam vacuum of the LHC [17] could only measure the electron flux. The energy spectrum of electrons up to 250 eV is measured with the collector at $+50$ V, while the grid is ramped from 0 V to -250 V. The full spectrum in Fig. 10 shows no significant contribution above about 10 eV.

In the upstream and downstream warm section the measured total flux originates from electrons with energies below 5 eV, with the peak at 1 eV and the half maximum at 3 eV. In the cold section the peak at 1 eV is much broader and has a different shape. This is demonstrated in Fig. 11. Assuming that the same contribution at 1 eV is present in all three sections, the spectrum in the cold section is split in two parts (Fig. 11). One part is a peak at 1 eV with the same shape as in the warm sections. The remaining part is a smaller peak at around 5 eV with a FWHM of about 6 eV. Because of this additional contribution the measured electron flux in the cold section is higher than in both

warm sections. This leads to the conclusion that the cryosorbed gas layer in the cold section produces electrons with an energy of about 5 eV.

Using a relatively simple model the heating power P_{beam} is given by $P_{\text{beam}} = \Delta W \cdot \dot{N}$, where $\dot{N}$ is the number of electrons per second hitting the cold liner and ΔW is the transferred energy [2]. Considering the above parameters at a beam current of 350 mA, assuming a 50% transparency of the grid and a uniformly distributed flux of electrons, and remembering that the ratio of the cold surface to the surface of the slits is about 130, the resulting heat load is less than 1 mW. Even if it cannot be excluded that the low energy electrons are not distributed equally, and therefore do not hit the liner where the slots to the RFAs are, this result indicates that low energy electrons are not responsible for the heating of the COLDDIAG liner.

In all three sections of COLDDIAG no significant variation of the electron flux is observed as a function of bunch length and bunch spacing. This supports the assumption that the origin of the measured low energy electrons is not the electron beam directly, but reflected
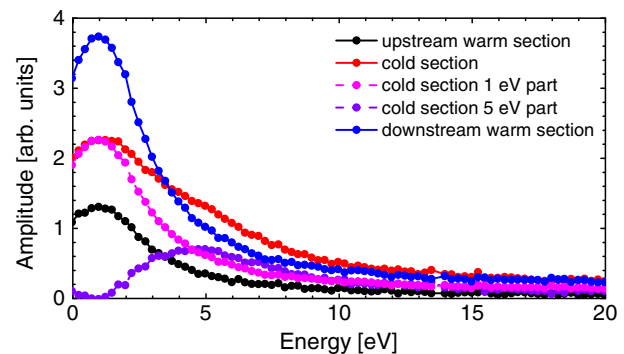

FIG. 11. Energy spectra of negatively charged particles (electrons) between 0 and 20 eV (energy resolution: 0.25 eV), hitting the chamber walls in each of the three sections of COLDDIAG with 250 mA and 900 bunches. The shape of the spectra is independent on the beam current. The energy spectrum in the cold section is split into a peak at 1 eV, proportional to the peaks in the warm sections, and the remaining part.

synchrotron radiation from the upstream bending magnet.

E. Temperature distribution on the liner

The temperature distribution on the cold liner has been monitored with 16 temperature sensors distributed along the bottom and top of the liner.

The temperature distribution on the liner is shown in Fig. 12 without beam and with a stored electron beam with 300 mA and 685 bunches, while keeping the cooling connection from the cryocooler to the liner at 20 K powering the heaters on the liner itself (upper plot), and without using the heaters (lower plot). The measurements show that the presence of the electron beam changes the temperature distribution on the cold liner.

In order to investigate the possibility of specific heating patterns leading to the observed temperature distribution on the liner, heat transfer simulations were performed using the finite element method. The simulations show that the observed temperature distribution on the cold liner cannot be explained by large gradients in the heat deposited at the inner surface of the liner, because the good heat conductivity of copper prevents large enough temperature gradients over such small distances [18]. A possible explanation for the temperature differences is a difference in thermal contact between temperature sensor and liner.
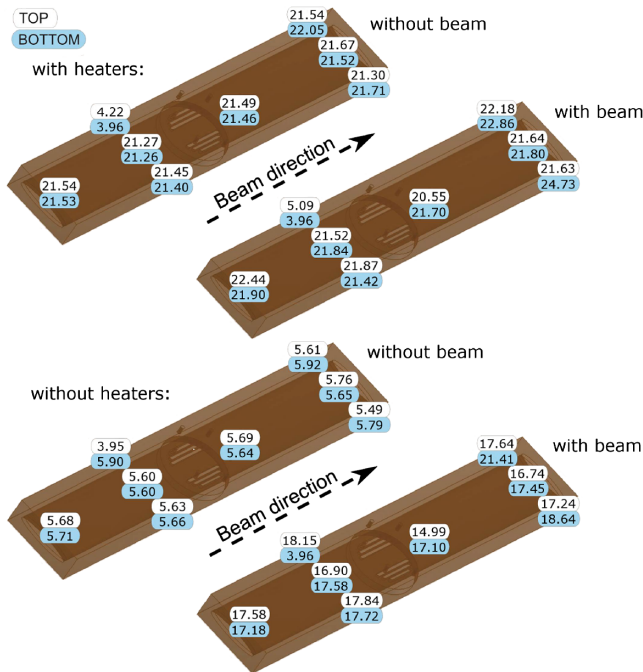

FIG. 12. The temperature distribution on the cold liner without beam and with a stored electron beam with 300 mA and 685 bunches, while keeping the cooling connection from the cryocooler to the liner at 20 K powering the heaters on the liner itself (upper plot), and without using the heaters (lower plot).

Additionally at high beam currents noise seems to affect the reading of the temperature sensors.

III. LONGITUDINAL IMPEDANCE BENCH MEASUREMENTS

Since the analysis of the data taken with COLDDIAG and discussed in the previous section were not conclusive, further investigations have become necessary in order to find the source of the measured beam heat load. The measurement of the longitudinal beam coupling impedance through the resonator method, particularly suited for the determination of small impedances (few Ω) [19,20] was used.

A. Experimental setup and method

A device under test (DUT), such as a reference tube or the COLDDIAG liner, is transformed into a resonator (see Fig. 13) by closing it with copper end plates, either integrated into a flange or pressed directly against the ends. At each end plate, (coaxial) measurement cables are connected through a SubMiniature version A-pin-connector, which couples into the resonator through a 3 mm pin (copper beryllium with 50 μm gold finish, 1.3 mm diameter) at the end of the coaxial feedthrough. The isolation material inside the connector is Teflon. Inside the DUT a copper rod (3.2 mm diameter, 99.9% purity) is centered to create a TEM line resonator. The centering is done using support pieces made from Teflon, the same material used inside the connectors. Its influence on the resistive part of the impedance is negligible. The length of the inner conductor is chosen in such a way that the coupling gap to the connector pin is 6 mm on each side. This value allows for an acceptable signal-to-noise ratio at low frequencies, where the noise floor is at -120 dB, while the coupling at high frequencies is still small enough to meet the requirement of weak coupling [19].

All measurements are performed with a 2-port vector network analyzer (Anritsu ShockLine™ MS46322A) in the frequency range between 1 MHz and 14 GHz. The measurement procedure is not possible for frequencies above the beam pipe cutoff, which is around 15 GHz for the elliptical cross section under study. Additionally, the capacitive coupling of the inner conductor to the pin
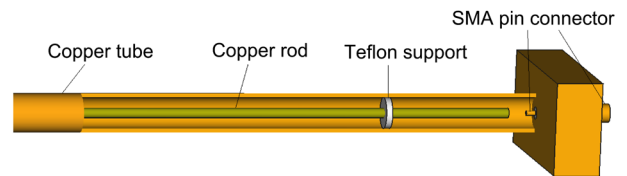

FIG. 13. Basic setup of the resonator method for impedance determination. A cut through the outer conductor (copper tube) shows the Teflon support and the capacitive coupling at one end of the resonator.

connectors, which is required to be weak for the measurement method, is getting stronger approaching the beam pipe cutoff. This effect has to be taken into account for the interpretation of the results above around 10 GHz.

The transmission S_{21} has been measured in a 16 MHz window centered at each resonance, giving a frequency resolution of 1 kHz. For each peak the transmission S_{21} and the frequency f_{res} at the maximum is determined, as well as the full width half maximum Δf. The real part of the longitudinal impedance $\text{Re}(Z)$ is

$$\text{Re}(Z)\left[\frac{\Omega}{m}\right] = 2Z_L \cdot \alpha, \qquad (4)$$

where α is the attenuation of the structure and Z_L the characteristic impedance. For a circular beam pipe $Z_L = 60\Omega \cdot \ln\frac{D}{d}$, which is the well-known expression for a coaxial line, with d the diameter of the inner conductor and D the diameter of the outer one. If the shape is different, an additional geometric factor has to be included in the logarithm. Regarding the characteristic impedance Z_L, the elliptical cross section chambers with the ratio of the semiaxes of $1/6$ are well approximated by parallel plates, adding a factor 1.27 in the logarithm $[Z_L = 60\Omega \cdot \ln(1.27\frac{D}{d})]$ [21]. We verified this factor experimentally by measuring the surface impedance of two copper tubes with the same surface roughness, one with circular and one with elliptical cross section with the smaller semiaxes equal to the radius of the circular one. The attenuation due to the structure itself $\alpha = \alpha_m - \alpha_w$ is the difference between the measured attenuation α_m and the attenuation due to the inner conductor α_w, depending on the skin effect and the geometry. The measured attenuation factor is

$$\alpha_m = \frac{\pi f_{\text{res}}(1 - |S_{21}|)}{cQ_L}, \qquad (5)$$

where f_{res} is the resonance frequency, c the speed of light, and $Q_L = f_{\text{res}}/\Delta f$ the loaded quality factor. For a circular coaxial line the attenuation α_w is given by

$$\alpha_w = \sqrt{\pi\rho_w\epsilon f_{\text{res}}} \frac{60\ \Omega}{dZ_L} \qquad (6)$$

being ϵ the permittivity and ρ_w the resistivity of the inner conductor.

In order to obtain the impedance $\text{Re}(Z)$ in Ω for each device, the $\text{Re}(Z)$ in Ω/m from Eq. (4), is multiplied by its length L.

A drawback of this method is that the impedance can only be determined at the resonant frequencies of the structure, which depend mainly on its length (dimension along beam direction). For a resonator of length L the resonant modes are defined by

$$f_{\text{res}} = n \cdot \frac{c}{2L}, \qquad (7)$$

where f_{res} is the resonant frequency, n is the mode number, and c is the speed of light. For a length of 0.5 m the fundamental mode ($n = 1$) is at 300 MHz and thus the points where the impedance can be evaluated are separated by 300 MHz. The accuracy of the measured impedance $\text{Re}(Z)$ at the different resonant frequencies is mainly affected by the accuracy of the transmission S_{21}, which is about 0.1 dB or 1%, and by the determination of the resonance width Δf, which is estimated conservatively to be 1% as well. The center frequency of a resonance peak can be determined very precisely ($<10^{-4}$) and it is assumed to be without error in this analysis. Errors introduced by a misalignment of the inner conductor have been studied by shifting the inner conductor off center. Closely related to this are errors introduced by unequal coupling. Below 10 GHz this error is negligible, because the reflection is close to 0 dB. Above 10 GHz the measurements are affected by coupling and are excluded.

The cold section of COLDDIAG is studied in three steps, allowing to differentiate between the impedance generated by the liner itself (490 mm), the thermal transitions from the cold liner to the 50 K shield (554 mm) and the finger bellows from the 50 K shield to the warm sections (850 mm, see Fig. 14).

B. Results

The results for the three sections indicated in Fig. 14 and described above are shown in Fig. 15 and compared with the predicted normal skin effect for an elliptical beam pipe with the same dimensions as the 490 mm cold section. The measurements for the three sections were performed at room temperature.

Only the 850 mm long section including all transitions could be measured also at 20 K, since the copper end plates were integrated into end flanges. The cryostat was cooled down to 4 K, and to be comparable to the beam heat load measurements, the liner temperature was adjusted to 20 K using the heaters on the liner. The small differences in the measurements performed at room temperature (blue dots) and at 20 K (cyan dots) can be attributed to mechanical changes during cooling. The main contribution to the
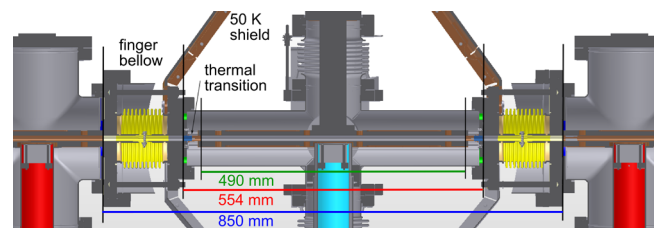

FIG. 14. Cut through the COLDDIAG cold part. Indicated are the three sections on which impedance measurements were performed.
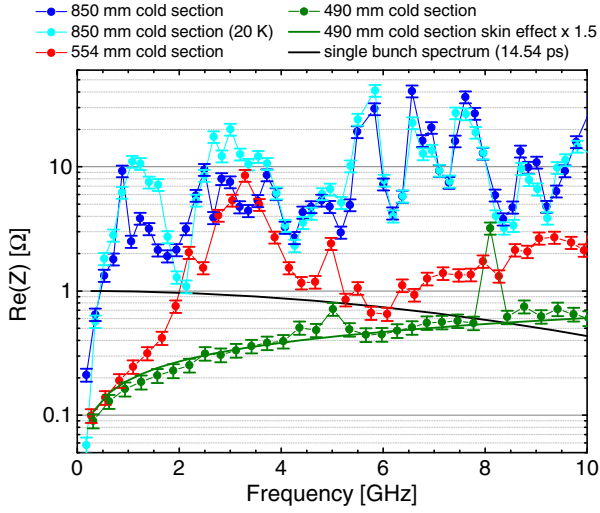
FIG. 15. Comparison between the impedance measurements on the three different sections of COLDDIAG as shown in Fig. 14 and the predicted normal skin effect for an elliptical beam pipe with the same dimensions as the 490 mm cold section, and multiplied by a factor of 1.5, which takes into account the surface roughness. The black line shows the normalized single bunch spectrum for 300 mA beam current in 900 bunches, assuming a Gaussian bunch with a bunch duration of $\sigma = 14.5$ ps.

impedance is here due to the rf bellows and flange connections, which are believed to be responsible of the several peaks measured.

The measured surface impedance on the 490 mm long section (green dots) can be explained as due to the skin effect including the effect of surface roughness (green solid line). The surface corrugations can increase the effective length of the beam pipe: in this case the predicted resistive wall impedance for an ellipse with the same dimensions as the cold liner has been multiplied by a factor of 1.5 [22].

The 554 mm cold section includes the thermal transitions from the shield at 50 K to the 4–20 K liner. In this case (red dots) the impedance is dominated by a broad peak centered around 3 GHz, and two less pronounced ones centered around 7 and 9 GHz, to be associated with the geometrical impedance of the thermal transitions superimposed to the resistive wall impedance.

Assuming a Gaussian bunch spectrum, the measured impedance can be used to calculate the power P_{loss} lost by the electron beam up to the measured frequency f:

$$P_{\text{loss}}(f) = \frac{2I^2}{N f_0} \cdot 2 \int_0^f \text{Re}(Z)(f') \exp{-(2\pi f' \sigma)^2} \mathrm{d}f', \quad (8)$$

where N is the number of bunches, I the average beam current, and $f_0 = 533.818$ kHz the revolution frequency. This expression holds in the absence of sharp resonant modes, for fills with equally spaced bunches and when the bunch spacing is much larger than the bunch duration.

The power lost by the electron beam up to the measured frequency f for the different parts described above, and for which the impedance is shown in Fig. 15, is reported in Fig. 16. Since above 10 GHz the impedance measurement is affected by coupling and the integral in Eq. (8) is suppressed due to the bunch spectrum, we approximate the values of $P_{\text{loss}}(10 \text{ GHz})$ as the total measured power losses due to impedance.

In Fig. 16 it is shown that the beam heat load measured in the cold section at the DLS with the cold liner at 20 K is almost the same as the power losses calculated from the measured impedance at room temperature in the section including the 4–20 K cold liner and the thermal transitions, connecting it to the 50 K shield. The impedance of the 490 mm liner measured at room temperature contributes only with 1 W to the measured value with beam of 4.3 ± 0.1 W for 900 bunches at an average beam current of 300 mA. The measured beam heat load is in agreement within less than 1 W with the power losses due to the measured impedance of the 554 mm long liner. The measured beam heat load can therefore be attributed to the geometrical impedance of the thermal transitions connecting the 50 K shield to the 4–20 K liner.

In order to make a more accurate comparison between the measured power losses $P_{\text{loss}}^{\text{im}}$ due to the impedance at room temperature and the power losses P_{beam} measured with beam with the liner at 20 K, the difference of the losses due to the normal skin effect $P_{\text{loss}}^{\text{sk}}$ at room temperature and the ones due to the anomalous skin effect $P_{\text{loss}}^{\text{sk}}$ in cold conditions needs to be considered:

$$P_{\text{loss}}^{\text{im-cor}} = P_{\text{loss}}^{\text{im}} - P_{\text{loss}}^{\text{sk}} + P_{\text{loss}}^{\text{an}}. \quad (9)$$
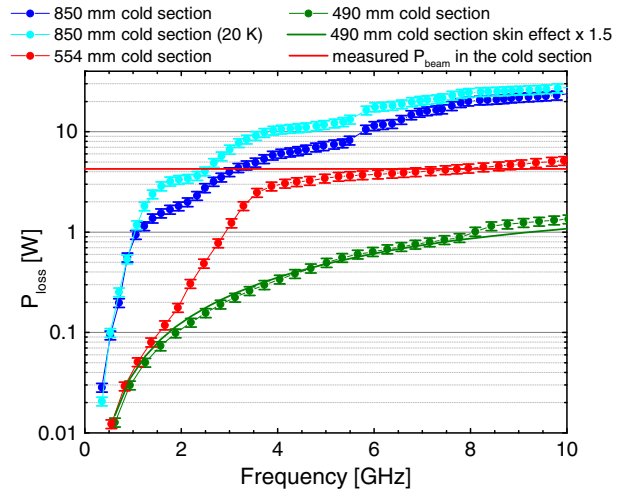

FIG. 16. The power lost by the electron beam up to the measured frequency f using the impedance in Fig. 15, assuming the same beam properties as for the measured beam heat load P_{beam} in the cold section (red solid line): 300 mA average beam current with 900 bunches and a bunch length of 14.5 ps.
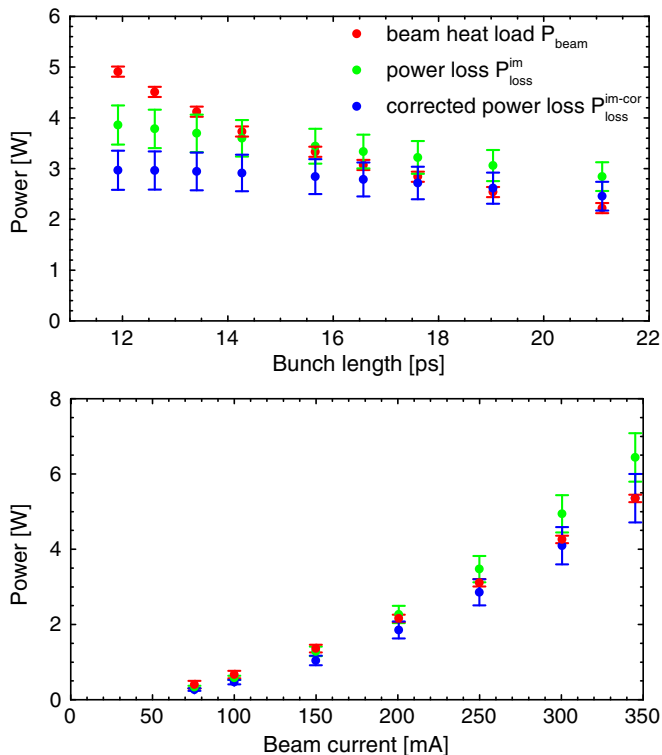
FIG. 17. Comparison between the power losses due to the impedance up to 10 GHz in Fig. 15 and measured beam heat load for 250 mA beam current and 900 bunches with different bunch lengths (top) and a beam current ramp with 900 bunches (bottom). The blue points are corrected by the difference between normal and anomalous skin effect ($RRR = 200$).

Taking this into account, a comparison between the measured power losses P_{loss}^{im}, the one corrected $P_{loss}^{im\text{-}cor}$ and the measured beam heat load is made in Fig. 17 for a filling pattern with 900 bunches as a function of the bunch length (top) and as a function of the average beam current I (bottom).

As a function of bunch length the corrected power loss is lower than the measured beam heat load for bunch lengths below 15 ps. An explanation for this behavior is that for smaller bunch lengths the single bunch spectrum gives a larger contribution at high frequencies, and we considered the contribution to the power losses only up to 10 GHz, neglecting the contribution above this frequency.

As a function of beam current the corrected power loss is in excellent agreement with the measured beam heat load. This result offers an explanation to the observed beam heat load.

IV. DISCUSSION

The beam heat load measured on the cold liner of COLDDIAG at the DLS has been studied as a function of several parameters of the machine, such as bunch length, bunch charge, and number of bunches, as well as by changing some of the COLDDIAG liner parameters, such as the temperature and the pressure.

In order to investigate electron bombardment as a heating mechanism the pressure and gas content have been monitored in COLDDIAG. Moreover, RFAs to measure the flux and energy spectrum of the charged particles hitting the wall have been installed in the two warm sections as well as in the cold one. The sensitivity of the pressure measurements is limited by outgassing in the areas where the gauges are installed. Within the sensitivity achieved, no correlation between the beam heat load and the pressure has been observed. This is different from the observations performed at ANKA with the superconducting undulator developed with ACCEL GmbH [2], where a correlation between beam heat load and pressure rise, which can be explained only by electron multipacting [23], was observed. This might be due to the fact that, while at ANKA the superconducting undulator cold bore was directly hit by synchrotron radiation, the COLDDIAG cold liner is screened from direct synchrotron radiation. Indirect synchrotron radiation can still hit the liner and create the photoelectrons, detected with the RFAs, without significantly contributing to molecule desorption. The linear dependence of the detected electron flux with beam current indicates that only photoelectrons are created and no multipacting takes place. The detected electron flux is less than 1 mW and much smaller than the measured beam heat load of several W, suggesting that the bombardment of the cold liner walls with low energy electrons is not the responsible mechanism for the beam heating observed.

The setup used for the measurements of the spectrum of the low energy electrons impinging the cold liner has been for the first time applied in COLDDIAG. This might be of interest for diagnostics applications in cold bore beam chambers exposed to synchrotron radiation, such as the Large Hadron Collider (LHC) [24] running at CERN and the Future Circular Collider (FCC) [25], under study as possible successor of the LHC.

The dependence of the measured beam heat load on the bunch length, bunch charge and number of bunches is consistent with a heating mechanism caused by a broadband impedance, due to the geometry or resistive wall heating. As shown in Fig. 1, the beam heat load predicted considering only resistive wall heating cannot explain the observed values.

The major contribution to the measured beam heat load can be attributed to the geometrical impedance of the thermal transitions between the shield at 50 K and the 4–20 K liner, described in detail in Ref. [6]. This has been demonstrated by off-line measurements of the longitudinal beam coupling impedance through the resonator method performed at KIT after removal of COLDDIAG from the DLS. The losses determined by the impedance bench measurements and the ones due to the beam show excellent agreement above 15 ps. Below bunch lengths of 15 ps, the

disagreement between the two measurements increases since we neglected the contribution to the losses above 10 GHz for the power loss determined by the impedance, and the contribution of the bunch spectrum at higher frequencies increases by reducing the bunch length. Particular care in the design, in manufacturing and assembling the thermal transitions has been taken in order to minimize the steps and the tapering angles. Mechanical tolerances might be responsible for the presence of asymmetry in the extremely shallow tapered sections and in the steps of about 10 μm constituting the thermal transitions [26]. On one side it is quite challenging to measure the geometrical configuration after installation with precisions of few μm. On the other side it is very demanding, even in case the geometry would be known with the required accuracy, to compute the impedance of such a structure with bunch lengths in the range of the ones at the DLS, with programs as Computer Simulation Technology [27] due to meshing and memory limitations.

V. CONCLUSIONS

The major contribution to the electron beam heat load measured with COLDDIAG at the DLS can be attributed to the impedance of the thermal transitions connecting the 50 K shield with the 5–20 K liner. The results obtained lead to important implications for the cryogenic design of superconducting undulators. In order to avoid electron bombardment effects, as observed at ANKA with the superconducting undulator developed with ACCEL GmbH, it seems to be sufficient, at least for electron machines, to screen the cold liner from direct synchrotron radiation. For direct beam heat load to a cold liner a conservative calculation of resistive wall heating is sufficient, taking into account the effect of surface roughness. Besides introducing heat from higher temperature regions, thermal transitions can be the source of additional heat intake due to imperfections in the geometric design. In order to reduce the beam heat load to the cold liner, care has to be taken in the design of the thermal transitions. It is unavoidable to include in the beam pipe inside the cryostat a region which allows to compensate the change in length of the beam pipe due to thermal shrinking: this is done by bellows using a shield for rf fields. The shield for rf consists of two tubes, which should be in very good electrical contact. The rf shield ineluctably includes in the beam pipe a taper, even if shallow, and steps, even if small ($\sim$100 μm). It is crucial to move these changes of the cross section to the region between 50 K and room temperature, in order to intercept the beam heat load produced by their impedance before the cold section.

[1] E. Wallén and G. LeBlanc, Cryogenic system of the MAX-Wiggler, Cryogenics **44**, 879 (2004).

[2] S. Casalbuoni, A. Grau, M. Hagelstein, R. Rossmanith, F. Zimmermann, B. Kostka, E. Mashkina, E. Steffens, A. Bernhard, D. Wollmann, and T. Baumbach, Beam heat load and pressure rise in a cold vacuum chamber, Phys. Rev. ST Accel. Beams **10**, 093202 (2007).

[3] N. Mezentsev and E. Wallén, Superconducting Wigglers, Synchrotron Radiat. News **24**, 3 (2011).

[4] J. C. Schouten and E. C. M. Rial, Electron beam heating and operation of the cryogenic undulator and superconducting wigglers at Diamond, *Proceedings of the 2nd International Particle Accelerator Conference, San Sebastián, Spain* (EPS-AG, Spain, 2011).

[5] Y. Ivanyushenkov *et al.*, Development and operating experience of a short-period superconducting undulator at the Advanced Photon Source, Phys. Rev. ST Accel. Beams **18**, 040703 (2015).

[6] S. Gerstl, R. Voutta, S. Casalbuoni, A. W. Grau, T. Holubek, D. Saez de Jauregui, R. Bartolini, M. P. Cox, E. C. Longhi, G. Rehm, J. C. Schouten, R. P. Walker, G. Sikler, M. Migliorati, and B. Spataro, Cold vacuum chamber for diagnostics: Instrumentation and first results, Phys. Rev. ST Accel. Beams **17**, 103201 (2014).

[7] http://www.diamond.ac.uk/Science/Machine.html.

[8] G. Rehm, A. Morgan, and C. Thomas, Beam diagnostics systems for the Diamond Synchrotron Light Source, in *Proceedings of the 9th European Particle Accelerator Conference, Lucerne, 2004* (EPS-AG, Lucerne, 2004).

[9] S. A. Heifets and S. A. Kheifets, Coupling impedance in modern accelerators, Rev. Mod. Phys. **63**, 631 (1991).

[10] A. Chao, *Physics of Collective Beam Instabilities in High Energy Accelerators* (John Wiley & Sons, Inc., New York, 1993).

[11] B. Podobedov, Resistive wall wakefields in the extreme anomalous skin effect regime, Phys. Rev. ST Accel. Beams **12**, 044401 (2009).

[12] Instruments, MKS, http://www.mksinst.com/docs/UR/423-specifications.aspx.

[13] K. Bernhardt, Vacuum Technology Compendium, Pfeiffer Vacuum GmbH, 2013.

[14] http://www.pfeiffer-vacuum.de.

[15] S. Gerstl, S. Casalbuoni, A. Grau, T. Holubek, D. Saez de Jauregui, R. Voutta, R. Bartolini, M. P. Cox, E. C. Longhi, G. Rehm, J. C. Schouten, R. Walker, M. Migliorati, and B. Spataro, Beam heat load measurements with COLD-DIAG at the Diamond Light Source, in *Proceedings of the 4th International Particle Accelerator Conference, IPAC-2013, Shanghai, China, 2013* (JACoW, Shanghai, China, 2013), p. 2135.

[16] Tektronix GmbH, Keithley Instruments Inc., 2013, http://www.keithley.de/.

[17] V. Baglin, I. R. Collins, and B. Jenninger, Performance of a cryogenic vacuum system (COLDEX) with an LHC type beam, Vacuum **73**, 201 (2004).

[18] R. Voutta, Ph.D. thesis, Karlsruhe Institute of Technology, Karlsruhe, Germany, 2016.

[19] F. Caspers and T. Scholz, Resonator method for impedance determination, Part. Accel. **50**, 125 (1995).

[20] T. Kroyer, F. Caspers, and E. Gaxiola, Report No. AB-Note-2007-028, 2007.

[21] S. G. Pan, Characteristic impedance of a coaxial system consisting of circular and noncircular conductors, IEEE Trans. Microwave Theory Tech. **36**, 917 (1988).

[22] E. Hammerstad and O. Jensen, Accurate models for microstrip computer-aided design, *Microwave symposium Digest, 1980 IEEE MTT-S International* (IEEE, Washington, 1980), pp. 407–409.

[23] S. Casalbuoni, S. Schleede, D. Saez de Jauregui, M. Hagelstein, and P. F. Tavares, Can electron multipacting explain the pressure rise in a cold bore superconducting undulator?, Phys. Rev. ST Accel. Beams **13**, 073201 (2010).

[24] L. Evans and P. Bryant, LHC Machine, J. Instrum. **3**, S08001 (2008).

[25] M. Benedikt and F. Zimmermann, Future Circular Collider (FCC) Study, APS Forum on International Physics, Spring 2015 Newsletter 15 (2015); http://www.aps.org/units/fip/newsletters/201502/collider.cfm.

[26] S. Casalbuoni, M. Migliorati, A. Mostacci, L. Palumbo, and B. Spataro, Beam heat load due to geometrical and resistive wall impedance in COLDDIAG, J. Instrum. **7**, P11008 (2012).

[27] CST AG, http://www.cst.com/, Darmstadt Germany.